

The onset of shock-induced particle jetting

Kun Xue ^{a,*}, Haoran Cui ^a, Kaiyuan Du ^a, Xiaoliang Shi ^a, Yixiang Gan ^b, Chunhua Bai ^a



^a State Key Laboratory of Explosive Science and Technology, Beijing Institute of Technology, Beijing 100081, China

^b School of Civil Engineering, The University of Sydney, Sydney, Australia

ARTICLE INFO

Article history:

Received 27 September 2017
Received in revised form 9 April 2018
Accepted 24 May 2018
Available online 26 May 2018

Keywords:

Particle jetting
Dynamic jamming front
Unjamming
Discrete element method
Hele-Shaw cell
Pattern formation

ABSTRACT

The shock dispersal of particle shells or rings by radially divergent impulsive loads takes the form of coherent particle jets which have much larger dimensions from those associated with the constituent grains. In the present study, quasi-two-dimensional particle jetting is studied via both experiments based on a radial Hele-Shaw cell and numerical simulations using the discrete element method. Simulations agree well with the experiments in terms of the branched jet pattern and characteristic timescale for jet growth. Besides simulations reproduce the signature events defining the jet formation observed in experiments, specifically the initiation of incipient jets from the non-perturbed internal surface of ring, as well as the concurrent ramification and annihilation of jets. More importantly the particle-scale simulations reveal the physics underlying the jet inception. We found that the onset of particle jetting corresponds to the transition of the shock jammed band which homogeneously expands outwards to the unevenly spaced localized shear flows, or equivalently, unjamming of the dynamic jamming front.

© 2018 Elsevier B.V. All rights reserved.

1. Introduction

Particle jetting during the explosive or shock dispersal of particles has been widely observed in nature and many military applications, such as volcanic eruption, explosion of landmines, thermobaric explosion, high-speed intruder striking granular media, and particle jets impacting targets, etc. [1–9]. A typical configuration involves particle rings or shells being exposed to radially divergent blast or shock fronts [1–8]. The resulting expanding cloud of explosion or shock disseminated materials comprises of large particle agglomerates which protrude to finger- or spike-like particle jets. Predicting the jet number has been an active area of research which requires the fundamental understanding of the physics underlying the jet formation [3,4,6–8,10].

Several theories have been put forward to account for the explosion driven particle jetting, including the Richtmyer-Meshkov instability [10], brittle fracture mechanism [7] and dual particle jetting mechanism [11]. Whereas no consensus has been reached yet. Compared with the extensive investigations into the explosion driven particle jetting, there are quite limited efforts put into studying the particle jetting induced by moderate shock waves with a peak overpressure on the order of $O(10^4\text{--}10^6)\text{Pa}$ [4,8,12,13]. Although both cases feature the resembling jetting pattern, we argue that the two jetting instabilities occur in different time scales and more importantly are governed by fundamentally different mechanisms since shock consolidation of

particles which dominates the blast-particle interactions is negligible under weak shock loadings [13].

In the opposite extreme scenario, similar finger-like patterns are formed when particles are displaced by the gases, fluids and other particles in a quasi-static manner [14–17]. Specifically, Sandnes et al. present a unified description of emerging morphologies in granular mixtures injected by gases in the form of extended phase diagrams [15]. During the viscous regime the hydrodynamic interactions dominate at high flow rate. Viscous granular fingers result from the competition between the viscous fluid drag and the friction between grains and against the confinement [14,15]. Again this theory doesn't hold for the shock induced particle jetting since in the latter case the build-up of friction is absent due to the overwhelming inertial forces and the hydrodynamic interactions play a minor role in the shock interaction regime.

Combining the radial Hele-Shaw cell which is commonly used in studying the particle fingering and the shock tube, Rodriguez et al. investigated the formation of particle jetting in a quasi-two-dimensional configuration and derived empirical relations between the jet number and a variety of structural parameters [4,8]. The experimental work done by Rodriguez et al. is more focused on the well-developed jet structure after the jets penetrate the external surface of ring [4,8]. Our previous simulations based on the discrete element method (DEM) performed instead reveal particle scale dynamics of jet formation before the penetration using similar configurations [13]. We argue that the heterogeneous network of force chains formed in the shock compacted particles is responsible for the formation of fast- and slow-moving particle clusters around the internal perimeter observed

* Corresponding author.

E-mail address: xuekun@bit.edu.cn (K. Xue).

in experiments [4]. But the intricate interplay between the erratic force structure and the flow patterns is far from clear thanks to the constant destruction and re-construction of the network of force chains as a result of ever-changing particle packing.

The aim of the present work is to elaborate the physics defining the inception of shock-induced jets from the particle-scale perspective. To this end, the particle scale information regarding the evolution of particle contact forces and velocities is necessary, which can be accessed by DEM simulations. Experiments based on the same quasi-two-dimensional configuration were also carried out to validate the simulation results.

2. Numerical and experimental setup

Originally developed by Cundall and Strack [18], the DEM is a numerical scheme that has been successfully used to simulate the response of granular media by modeling the dynamic behavior of large assemblies of circular disks, spheres, and blocks [9,13,19–22]. The motion of each particle in the assembly is governed by the following equations

$$\begin{cases} m_i \frac{dV_i}{dt} = \sum_{j=1}^{n_i^c} F_{ij}^c + F_i^g + F_i^{ex} \\ I_i \frac{d\omega_i}{dt} = \sum_{j=1}^{n_i^c} M_{ij} \end{cases} \quad (1)$$

where V_i and ω_i denote the translational and angular velocities of particle i , respectively; F_{ij}^c and M_{ij} are the contact force and contact torque acting on particle i by particle j or the wall(s), respectively; n_i^c is the number of total contacts for particle i ; F_i^g is the gravitational force, and F_i^{ex} is other external force; m_i and I_i are the mass and moment of inertia of particle i . The Hertz-Mindlin contact law is employed in conjunction with Coulomb's friction law to describe the inter-particle contact behavior. Details of the contact model and the parameters used in the simulations are presented in Appendix I.

The particle packing is established by first letting free-falling spherical quartz sand particles settle by gravity in annular simulation boxes and allowing them to relax until the kinetic energy of assembly ceases to decrease. A series of particle rings were generated this way with the inner diameter normalized by the particle diameter, $\hat{D}_{in} = D_{in}/d_p$, ranging from 200 to 1600. The normalized width of ring, $\hat{w} = (D_{out} - D_{in})/(2d_p)$, was kept constant, $\hat{w} = 400$. The resulting short annular particle bands have the height 2–3 times the particle diameter. The friction between container walls (i.e., the top and bottom plates) and grains is negligible. Thus the three-dimensional effect becomes negligible.

In the present simulations, the shock loading is achieved by applying constant forces on particles residing along the internal perimeter as shown in Fig. 1. The magnitude of the force applied on each particle equals to the cross-section area of this particle multiplied by the overpressure, Δp_0 , which ranges from 0.5 to 10 bar. Also the applied force vector aligns with the local radial direction. Ref [4] compares the effects of overpressure profiles on the jet pattern and found no noticeable differences in patterns generated by the pressure jumps followed by a constant value or a rapid decline. A specific loading algorithm was invoked to mimic the penetration of pressurized gases trapped inside the particle ring into the bulk, which is manifested by particles clustering around the cusps of the disturbed internal surface persistently being subjected to the impulsive loads (see Fig. 1(b)). Details of the loading algorithm can be referred to Ref [13].

In order to verify the numerical results, we also performed experiments of the shock dispersion of the quartz sand ring using moderate shock waves. The quasi-two-dimensional configuration setup as schematized in Fig. 2 consists of a radial Hele-Shaw cell and a vertical shock tube similar to that used in Refs. [4, 8, 12]. The outlet of the shock tube is fitted vertically beneath the Hele-Shaw cell, matching the hole in the bottom plate with the same diameter. A concentric particle ring disposed around the bottom hole consisting of fine quartz grains with the average diameter of 50 μm is trapped between the top and bottom plates of the Hele-Shaw cell. The incident shock wave and the trailing pressurized gas flows bursting out of the shock tube hit the top plate and are forced through the gap between the top and

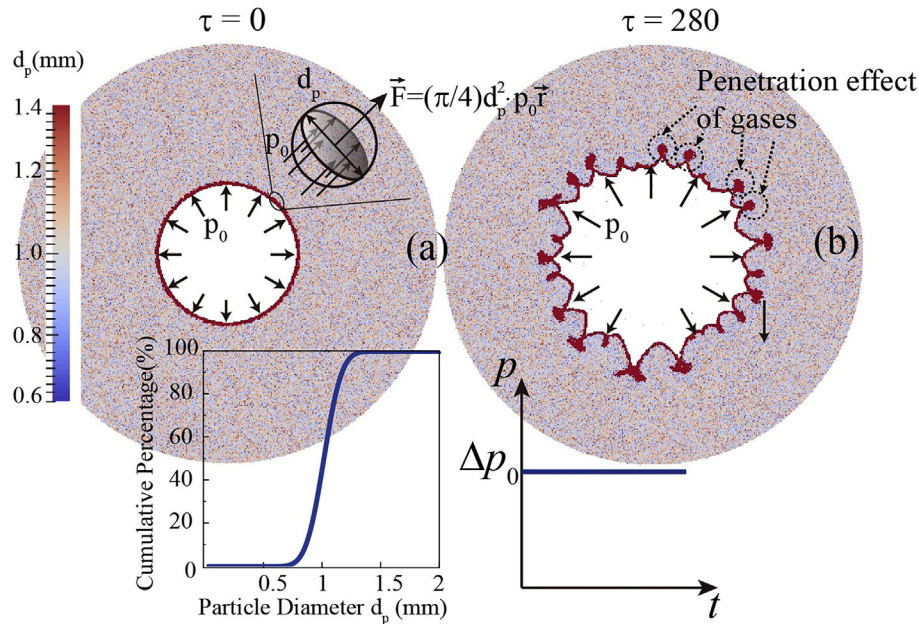


Fig. 1. Snapshots (top views) of the particle ring ($\hat{D}_{in} = 400$) before (a) and after (b) the loading. Particles in the innermost layers and clustering around the cusps of the internal surface (shaded red) are subjected to the radially directed constant forces which are proportional with the cross-section areas of the individual particles. The proportional factor is the peak overpressure Δp_0 . Insets of (a) and (b) represent the statistical distribution of particle diameter, d_p , and the profile of the impulsive load used in the simulations. (For interpretation of the references to colour in this figure legend, the reader is referred to the web version of this article.)

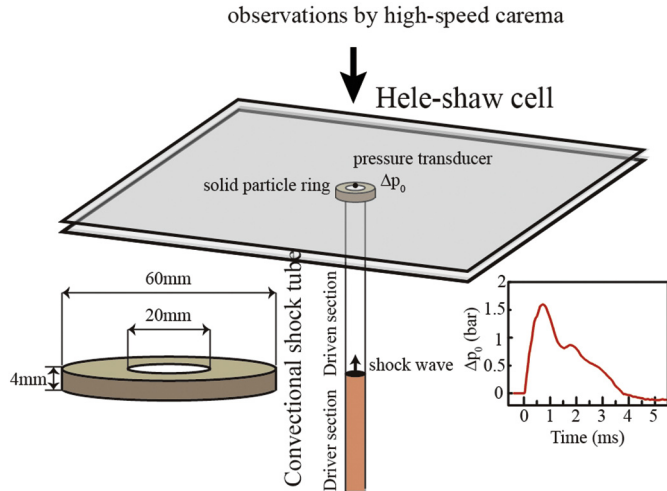


Fig. 2. Schematic of the quasi-two-dimensional configuration setup based on the Hele-Shaw cell.

bottom plates, whereby creating a radially divergent blast wave, i.e., an impulsive pressure jump followed by a rapid pressure decrease (see the inset of Fig. 2). Mach number of the incident wave varies from 1.07 to 1.48 with Δp_0 measured at the tube exit varying from 1.52 to 6.67 bar [12]. The particle dispersion is recorded by a high-speed camera (Photron SA5) with the frame rate of 10,000/s.

3. Results

Fig. 3 compares the experimentally observed and numerically derived snapshots of jet formation in particle rings with the same scaled geometries, $\hat{D}_{in} = 400$ and $\hat{D}_{out} = 1200$ at different scaled time. The scaled time, τ , is the time normalized by the propagation time of the incident wave through the width of ring, $\tau = t/t^* = t/(w/D)$, where D is the sound speed of quartz sand. The simulated jetting pattern exhibits well-identified branched finger-like jetting pattern analogous to that observed in the experiments [10]. Two characteristic events, namely the ramification of jets through tip-splitting and the elimination of jets can be found in both experiments and simulations throughout the jet formation (see Fig. 3).

Fig. 4(a) shows the typical growth histories of jets derived from both experiments and simulations with the identical key features. Particle jets undergo an early slow growth stage, then pick up some momentum until the tip-splitting takes hold. More importantly, the characteristic growth rate of jets derived from simulations agrees well with that obtained experimentally (see Fig. 4(b)). Note that the DEM simulations did not incorporate the complex hydrodynamic effects of gas-particle interactions, such as the viscous fluid drag, lubrication forces, long-range hydrodynamic interactions, and inhomogeneous Darcy gas fluxes, despite of the specific algorithm devoted to taking into account the penetration effect of pressurized gases (in Section 2). Thus the good agreement of the average jet growth rates derived from the experiment and simulation suggests that hydrodynamic effects only play a minor role in the shock-induced particle jetting. Actually these hydrodynamic effects take effect in much longer timescale and are largely retarded by the shock compaction. Both the average and maximum growth rates of jets, \bar{V}_{jet} and $V_{jet,max}$, increase with the peak overpressure as shown in Fig. 4(b).

4. Inception of shock-induced particle jets

In Sections 4 and 5, we take the jet formation in the ring with $\hat{D}_{in} = 400$ and $\hat{D}_{out} = 1200$ subjected to the impulsive load with $\Delta p_0 = 5$ bar as an example to describe how the initially

smooth internal surface of ring becomes disturbed. Immediately following the loading, a compacted annular band is formed around the internal perimeter and moves radially outwards. As shown in the Fig. 5(a), the radial profiles of azimuthally averaged packing fraction, $\phi(R,t)$, normalized by the peak saturation packing fraction, ϕ^* , in the early stage indicate a jammed disordered band with the packing fraction saturated at ϕ^* whose value was found to be around 0.55 in this quasi-two-dimensional configuration. Packing fraction gradually decreases across a dynamic jamming front delineated by the leading and trailing edges. The jammed band moves radially outwards with a uniform velocity across the width of the band as evidenced by the plateaus of the radial profiles of the coarse-grained velocity, $V(R,t)$, normalized by the maximum velocity, V_{max} (see Fig. 5(a)). The normalized velocity smoothly transits from the maximum value behind the trailing edge of the jamming front to almost zero beyond the leading edge of the jamming front.

In Fig. 5(b), we show the positions of the jamming front's leading edge R_{LJ} , trailing edge R_{TJ} , as well as the internal surface R_{in} , normalized by the particle diameter, as a function of time. At first instants, all three grow linearly with time at different rates such that the normalized thickness of the jammed band, \hat{w}_{jammed} , and the normalized width of the jamming front, $\hat{w}_{jamming}$, both grow with time. The trajectories of R_{LJ} , R_{TJ} and R_{in} undergo a kink simultaneously at a critical time $\hat{\tau} \sim 30$, afterwards increasingly deviating from the linear trajectories. The values of \hat{w}_{jammed} and $\hat{w}_{jamming}$ level off in later stages.

The azimuthally averaged velocities smooth out the circumferential fluctuations which may well be responsible for the discernable kinks in the trajectories of R_{LJ} , R_{TJ} and R_{in} . More importantly, the azimuthal fluctuations of velocities precede to any detectable instabilities emerging along the internal perimeter (see Fig. 3(a) and (f)). Fig. 6(a) shows the azimuthal profiles of normalized radial velocity fluctuations in the jammed band, $\Delta\hat{V}_r = (V_r - \bar{V}_r)/\bar{V}_r$, where \bar{V}_r is the azimuthally averaged radial velocity. A large number of randomized oscillations of $\Delta\hat{V}_r$ with small magnitudes at first two instants (see the top two panels in Fig. 6(a)) is indicative of the radially divergent uniform flows. But these irregular oscillations are rapidly reduced to a fraction of periodically spaced fluctuations with increased amplitudes (see the bottom two panels in Fig. 6(a)), and a consistent pattern emerges. The well-defined velocity peaks correspond to the fast-moving particle clusters herein, or equivalently localized shear flows.

In order to better visualize the transition from the homogeneous diverge flows to the localized shear flows, we plot the correlation coefficients of $\Delta\hat{V}_r$ at zero phase shift between two sequent instants, τ and $\tau + \Delta\tau$ ($\Delta\tau = 3.5$), as well as between τ and the end of transition ($\tau = 140$), referred to as $\chi_{Vr,0}(\tau, \tau + \Delta\tau)$ and $\chi_{Vr,0}(\tau, \tau = 140)$, respectively, as a function of τ (see Fig. 6(b) and (c), respectively). The coefficients are obtained through

$$\chi_{Vr}(\tau_1, \tau_2) = \frac{\sum_{m=1}^M (\Delta\hat{V}_r(\tau_1)_m - \langle \Delta\hat{V}_r(\tau_1) \rangle)(\Delta\hat{V}_r(\tau_2)_m - \langle \Delta\hat{V}_r(\tau_2) \rangle)}{\sqrt{\sum_{n=1}^M (\Delta\hat{V}_r(\tau_1)_n - \langle \Delta\hat{V}_r(\tau_1) \rangle)^2 \sum_{n=1}^M (\Delta\hat{V}_r(\tau_2)_n - \langle \Delta\hat{V}_r(\tau_2) \rangle)^2}} \quad (2)$$

where $\langle \Delta\hat{V}_r(\tau_1) \rangle$ and $\langle \Delta\hat{V}_r(\tau_2) \rangle$ are the azimuthal averages of $\Delta\hat{V}_r(\tau_1)$ and $\Delta\hat{V}_r(\tau_2)$, respectively. Note that χ_0 denotes the value of χ at the zero phase shift as indicated in the inset of Fig. 6(b).

A resembling trend can be identified from the temporal variations in both $\chi_{Vr,0}(\tau, \tau + \Delta\tau)$ and $\chi_{Vr,0}(\tau, \tau = 140)$. Before $\tau \sim 30$, low values of $\chi_{Vr,0}(\tau, \tau + \Delta\tau)$ and $\chi_{Vr,0}(\tau, \tau = 140)$ indicate a lack of persistent features in the azimuthal profile of $\Delta\hat{V}_r$, the homogeneous divergent flows maintained. Afterwards the substantial rises of $\chi_{Vr,0}(\tau, \tau + \Delta\tau)$ and $\chi_{Vr,0}(\tau, \tau = 140)$ suggest that a consistent azimuthal pattern

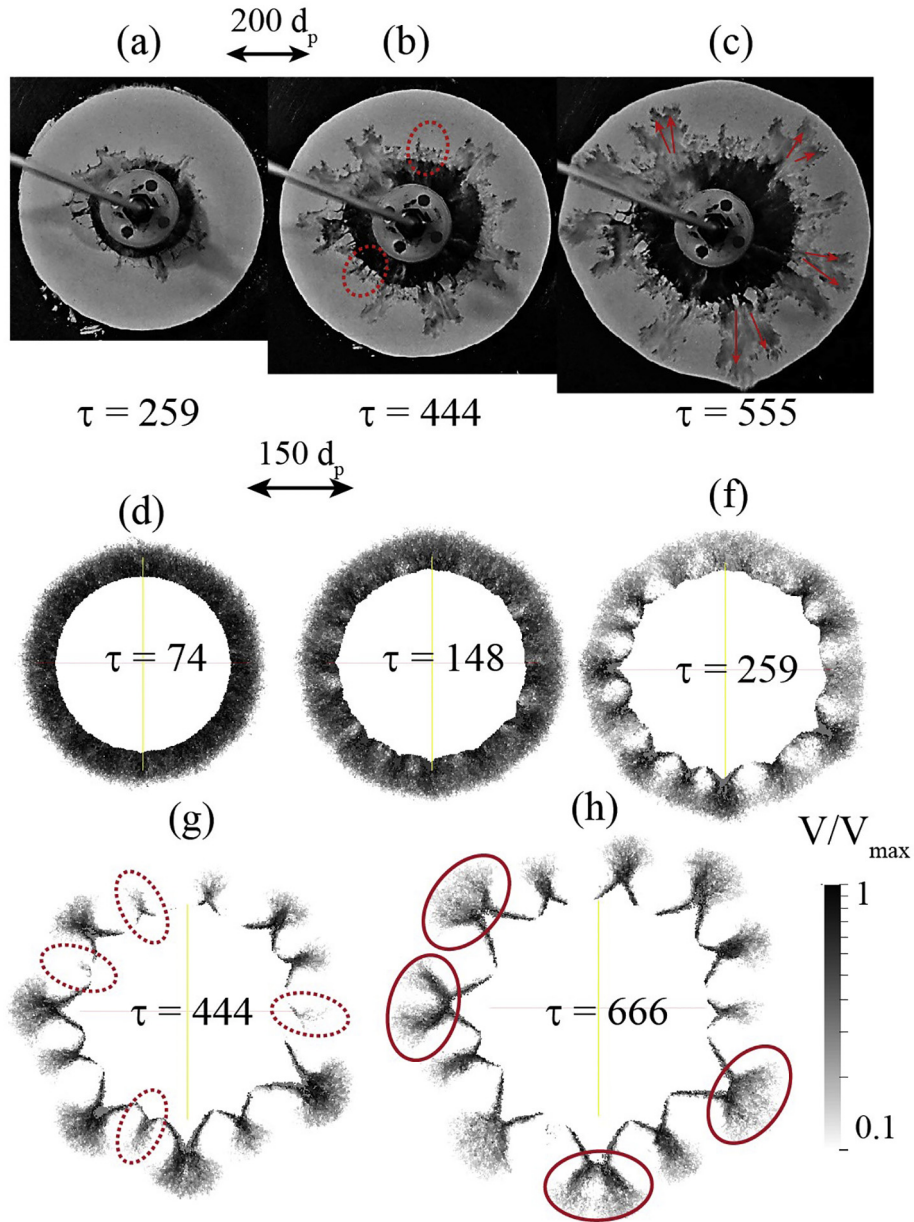


Fig. 3. Snapshots of shock dispersion of the particle ring ($\bar{D}_{in} = 400$ and $\bar{D}_{out} = 1200$) subjected to $\Delta p_0 = 1.7$ bar at different scaled times: (a)–(c) High-speed photos of experiments, where dashed circles and arrows indicate the annihilated and ramified jets, respectively; (d)–(h) The configurations of shock dispersed particle ring derived from simulations, with particles shaded according to the magnitude of the velocities. The dashed and solid circles in (g) and (h) indicate the annihilated and ramified jets, respectively.

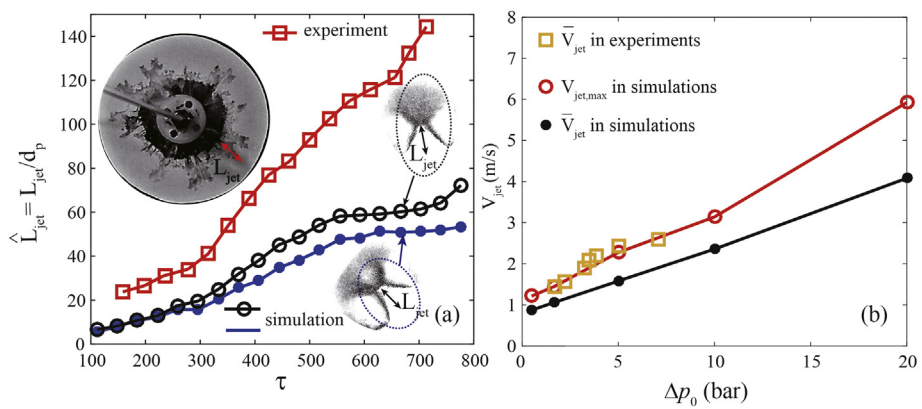


Fig. 4. (a) Typical growth histories of jets derived from simulations and experiments. Insets: high-speed photo of the shock dispersed ring (upper) and snapshots of two simulated incipient jets (the bottom two). (b) Variations in average and maximum growth rates of jets, \bar{V}_{jet} and V_{jet} , with increasing overpressure Δp_0 . Parameters in (a): $\bar{D}_{in} = 400$, $\bar{D}_{out} = 1200$, $\Delta p_0 = 1.7$ bar.

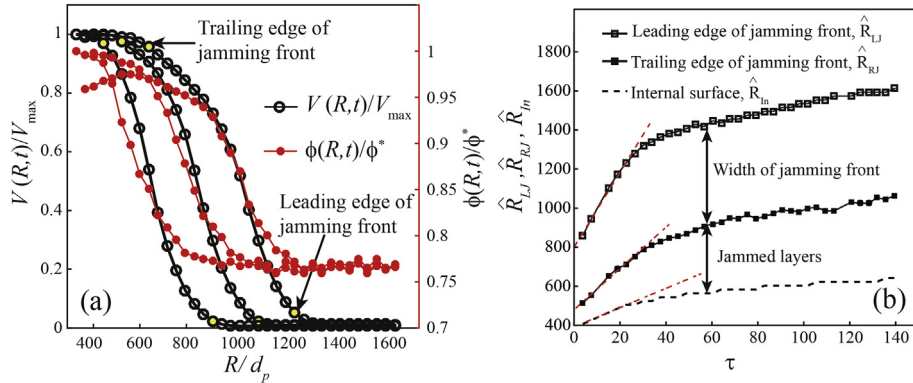


Fig. 5. (a) Radial profiles of the azimuthally averaged velocity normalized by the maximum velocity, $V(R,t)/V_{\max}$, and the azimuthally averaged packing fraction normalized by the peak saturation velocity, $\phi(R,t)/\phi^*$, at $\tau = 10.5, 18, 30$, from left to right. (b) Normalized radii of internal surface ($\hat{R}_{in} = R_{in}/d_p$), the trailing ($\hat{R}_{RJ} = R_{RJ}/d_p$) and leading edges ($\hat{R}_{LJ} = R_{LJ}/d_p$) of the jamming front as a function of normalized time.

of $\Delta\hat{V}_r$ is in the making. Obviously the transition from the homogeneous divergent flows to the localized shear flows in the jammed band, or equivalently the unjamming process, substantially decelerates the outward expansion of the jamming front as well as the internal surface since a considerable portion of shock energy is dissipated in the intensified localized flows.

5. Physics initiating the unjamming process

Understanding the physics underlying the unjamming process entails the knowledge of the heterogeneous force structure in the

shocked particles. Fig. 7(a) shows a typical snapshot of force network formed within the shocked particle layer. In contrast with the dense intricate network of force chains percolating the jammed band whereby jammed particles are tightly bound together, sparsely spaced and randomized long protruding force chains run through the jamming front. Consequently the clustering of force chains nucleated by these protruding chains is much more conspicuous across the width of the jamming front than within the jammed band, as supported by the much more pronounced fluctuations of contact densities (average number of contacts per particle) therein (see Fig. 7(b)). Similar rough protrusions extending from the dynamic jamming front have also been recognized in other studies [23].

These protruding finger-like agglomerates of force chains across the width of the jamming front channel the momentum into the bulk, activating a large number of small fast-moving particle clusters. The velocity differences across the boundary of the fast-moving particle clusters cause the particle rearrangement whereby micro voids are deposited in the neighborhood of the boundary, leading to reduced

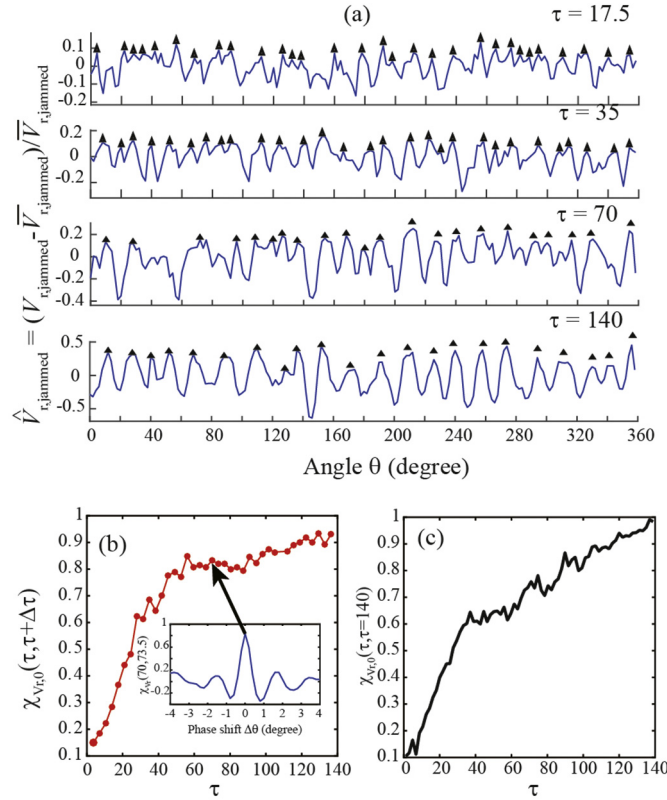


Fig. 6. (a) Azimuthal profiles of scaled radial velocity fluctuations, $\Delta\hat{V}_r$, at different times. (b–c) Temporal variations in the correlation coefficients of $\Delta\hat{V}_r$ at zero phase shift, $\chi_{V,0}$, between two sequent instants, and τ and $\tau = 140$, respectively. Inset of (b): variations of $\chi_{V,0}(\tau, \tau + \Delta\tau)$ with the phase shift.

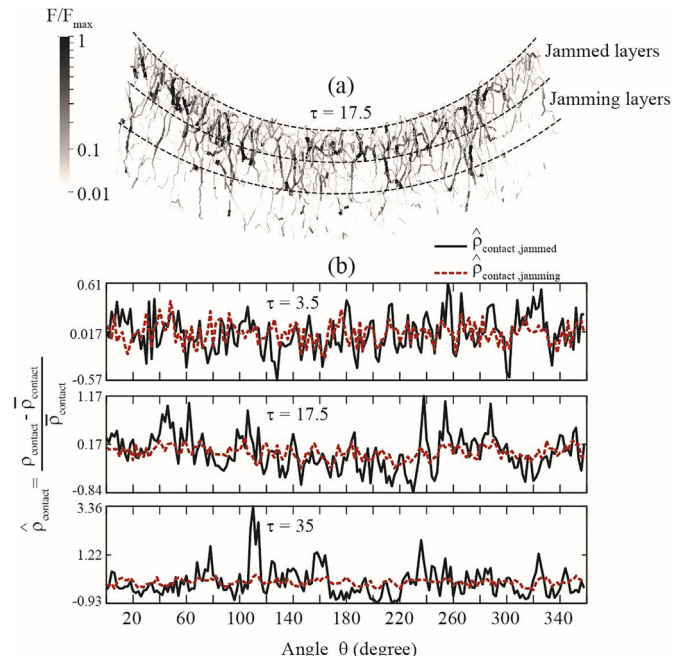


Fig. 7. (a) Snapshot of a part of force structure formed in shocked particles. (b) Azimuthal profiles of contact density fluctuations normalized by the azimuthally average contact density, $\hat{\rho}_{contact}$, in jammed and jamming layers at different times. Here the coarse-grained contact density is defined as the average number of contacts per particles.

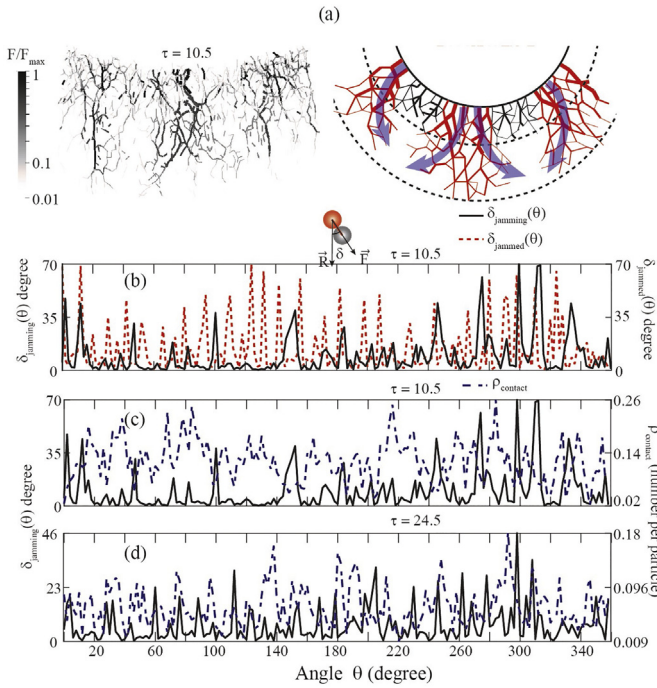


Fig. 8. Snapshot and the corresponding illustration of the force network in shocked particles. (b) Azimuthal profiles of the deflection angles of force chains, δ , as illustrated in the inset, across the jamming front (black solid line) δ_{jamming} and within the jammed layers (red dashed line) δ_{unjammed} at $\tau = 10.5$. (c) and (d): Azimuthal profiles of the deflection angles of force chains and the contact densities across the jamming front, δ_{jamming} and ρ_{jamming} , at $\tau = 10.5$ and 24.5 respectively. (For interpretation of the references to colour in this figure legend, the reader is referred to the web version of this article.)

local packing densities. Weakened lateral confinements experienced by the fast-moving particle clusters allow the transverse particle flows at the tips of fast-moving particle clusters as illustrated in the right panel of Fig. 8(a). Force chains accordingly deflect laterally. A handful of strongly deflected force chains can be identified from a segment of the snapshot of force chains in the left panel of Fig. 8(a). Deflected force chains further carry momentum into transverse flows.

The transverse particle flows coupling with lateral deflection of force chains aforementioned predominantly take place across the jamming front rather than within the jammed band, which can be corroborated by Fig. 8(b)–(d). Fig. 8(b) plots the azimuthal profiles of the coarse-grained lateral deflection of force chains in terms of the angle between contact force vector and the local radial orientation, δ , across the jamming front (δ_{jamming} , solid lines) and within the jammed band (δ_{unjammed} , dashed lines) prior to the onset of unjamming. A large number of spikes of δ_{unjammed} originate from the largely isotropic network of force chains within the jammed band. By contrast, a handful of conspicuous peaks of δ_{jamming} against relatively flattened background indicate strongly localized deflected force chains across the width of the jamming front. Not surprisingly these strongly deflected force chains stem from the boundaries of the agglomerates of force chains as suggested by the mismatch of peaks in the azimuthal profiles of contact densities and the deflection angles of force chains (see Fig. 8(c) and (d)).

If the deflected force chains stemming from two adjacent fast-moving clusters overlap with each other, two head-on transverse flows subsequently collide with each other so that an incipient vortex is formed as identified from the first snapshot of the velocity profiles in Fig. 9(a). These vortices first born within the jamming front rapidly move inward, canceling out the radial flows in their wakes and leading to localized shear flows (see Fig. 9(a)). Fig. 9(b) shows the evolutions of the azimuthal profiles of the absolute tangential velocities across the jamming front and the radial velocities in the jammed band, $V_{t,\text{jamming}}$ and $V_{r,\text{jammed}}$. With the unjamming process unfolds, the peaks of V_t ,

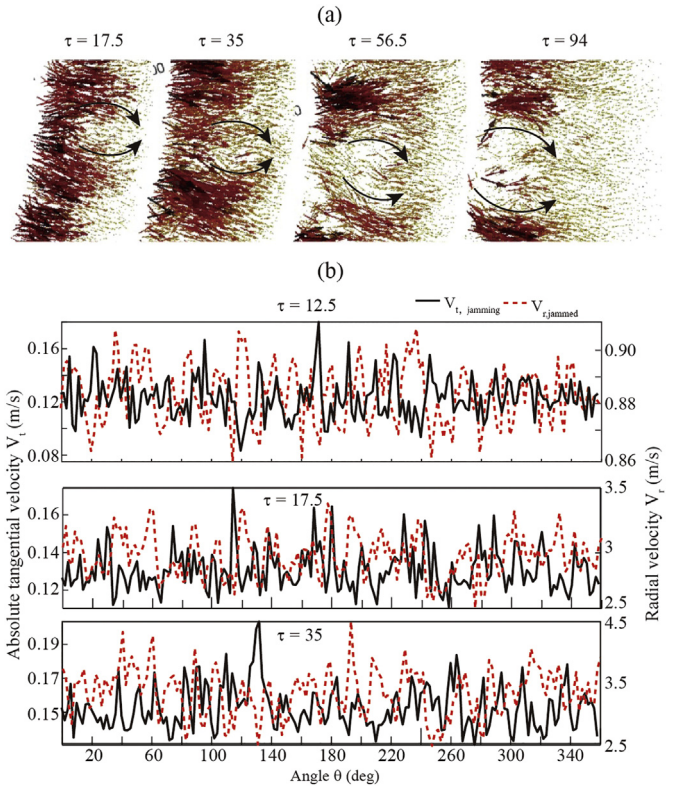


Fig. 9. (a) Snapshots of the velocity vector profiles in a segment of particle ring. The velocity vector is shaded according to the magnitude. (b) Azimuthal profiles of the absolute tangential velocities within the jamming front and radial velocities in the jammed layers, $V_{t,\text{jamming}}$ and $V_{r,\text{jammed}}$, at different times.

jamming increasingly coincide with the troughs of $V_{r,\text{jammed}}$, which is consistent with the argument that it is the inward propagation of vortices that unjams the jammed band, leading to the well separated localized shear flows. Alongside the inward motion, some strong vortices continuously grow transversely, annihilating a significant number of weak localized flows. As a result, only a fraction of localized flows can survive and grow into incipient jets.

6. Influences of structural parameters on the inception of jets

In this section, we examine the effects of a variety of parameters, including the peak overpressure Δp_0 , the gap between the top plate and the top surface of particle ring Δh , and the internal diameter of ring D_{in} on the pattern of incipient jets.

Fig. 10 shows the configurations of internal surfaces of rings at the end of the unjamming process in terms of the normalized radius fluctuations of particles constituting the internal perimeters, $\hat{\Delta R}_{\text{in}}(\theta) = (R_{\text{in}}(\theta) - \bar{R}_{\text{in}})/\bar{R}_{\text{in}}$. The peaks in the azimuthal profiles of $\hat{\Delta R}_{\text{in}}(\theta)$ correspond to the cusps of incipient jets. As indicated by Fig. 10(a) and (b), neither Δh nor Δp_0 has discernable effects on the number of incipient jets despite that the larger Δh and elevated Δp_0 can quicken the unjamming process. It is worth noting that there is substantial mismatch of the positions of incipient jets for the same particle ring with different Δh . The correlation coefficient at zero phase shift of azimuthal profiles of $\hat{\Delta R}_{\text{in}}(\theta)$ for these two cases is only 0.14. By contrast, the variations in Δp_0 in the studied range (0.5–10 bar) barely change the azimuthal distribution of incipient jets (see Fig. 10(b)). Table 1 lists the correlation coefficients at zero phase shift of azimuthal profiles of $\hat{\Delta R}_{\text{in}}(\theta)$ in cases with different Δp_0 . Therefore, the unjamming process which is closely related with the distinctive network of force chains is

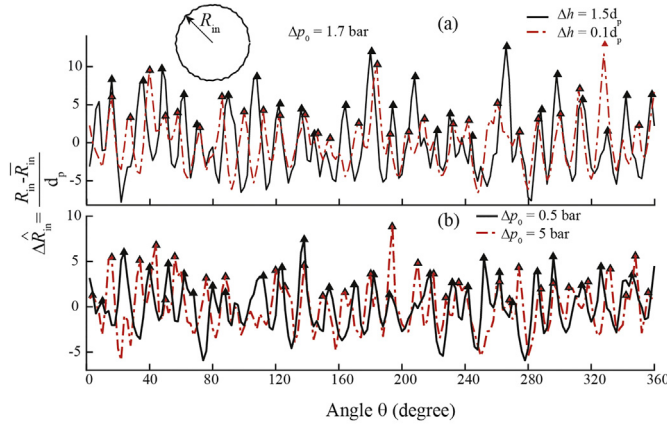


Fig. 10. Azimuthal profiles of the normalized radius fluctuations of particles along the internal perimeters of the rings with different Δh (a) and the rings subjected to loads with different Δp_0 (b). The configurations of the internal perimeters of rings (see the inset of (a)) are derived at the end of the unjamming process.

intricately dictated by the packing structures rather than the external loading conditions.

The number of incipient jets, N_{jet} , increases with the normalized internal diameter of ring, \hat{D}_{in} , as expected (see Fig. 12). But the N_{jet} vs \hat{D}_{in} curve increasingly lags behind the linear dependence, suggesting that the average spacing of incipient jets, w_{jet} (as defined in the inset of Fig. 11), increases with \hat{D}_{in} . The structure of force network and the interplay between neighboring localized flows are not fundamentally altered by the varying \hat{D}_{in} , implying the same unjamming physics in action. Accordingly the trajectories of the normalized displacements of the internal surface, $\Delta\hat{R}_{in}$, the leading and trailing edges of jamming front, $\Delta\hat{R}_{lj}$ and $\Delta\hat{R}_{Tj}$, follow the same respective trajectories regardless of \hat{D}_{in} as shown in Fig. 12(a). We argue that it is the geometric effect related with the curvature of the internal perimeter of ring that causes the increased w_{jet} with D_{in} . Fig. 12(b) illustrates the interplay between neighboring localized flows, in which the shaded elliptical areas represent the areas covered by the laterally deflected branches of force chains stemming from the protruding force chain agglomerates that are the backbones of localized flows. Only the influencing areas of neighboring localized flows overlap with each other, can the interplay between these localized flows take place. Since the unjamming timescale, the width of the jammed band and the jamming front at the onset of unjamming are invariable with varying D_{in} (see Fig. 12(a)), it is reasonable to assume a constant critical spacing between the centers of the rounded cusps of localized flows, $S_{jet,c}$ as illustrated in Fig. 12(b). The relation between w_{jet} and S_{jet} is proposed as follows

$$w_{jet} = R_{in,u} \cdot \frac{S_{jet,c}}{(R_{Tj,u} + R_{Lj,u})/2} \quad (3)$$

where $R_{in,u}$, $R_{Lj,u}$ and $R_{Tj,u}$ are the radii of the internal perimeter, leading and trailing edge of the jamming front at the onset of

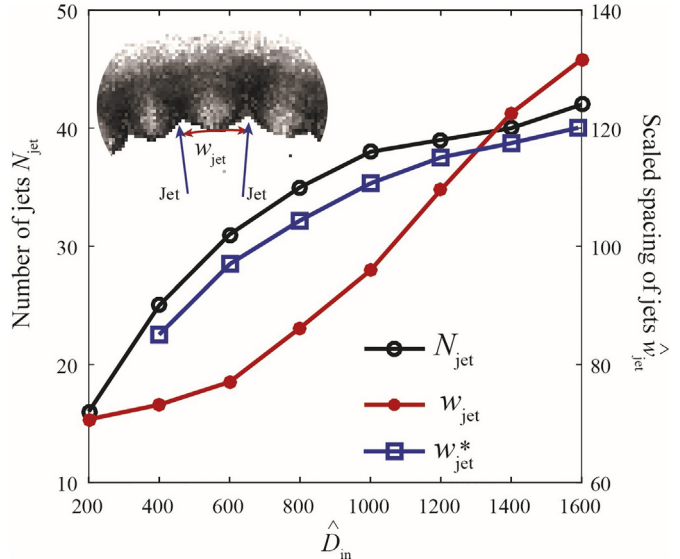


Fig. 11. Number of jets, N_{jet} , and the average spacing of jets, w_{jet} (derived from simulations) and w_{jet}^* (predicted theoretically), as a function of the normalized internal diameter of ring, \hat{D}_{in} .

unjamming, respectively. Here, $R_{in,u}$, $R_{Lj,u}$ and $R_{Tj,u}$ can be calculated from

$$R_{in,u} = R_{in} + \Delta R_{in,u}, R_{Lj,u} = R_{in} + \Delta R_{Lj,u}, R_{Tj,u} = R_{in} + \Delta R_{Tj,u}, \quad (4)$$

where $\Delta R_{in,u}$, $\Delta R_{Lj,u}$ and $\Delta R_{Tj,u}$ are the displacements of the internal perimeter, the leading and trailing edge of the jamming front at the onset of unjamming.

Thus the ratio of incipient jet spacings in rings with different internal radii, $R_{in,1}$ and $R_{in,2}$ is related with the ratio of $R_{in,1}$ and $R_{in,2}$

$$\frac{w_{jet,1}}{w_{jet,2}} = \frac{R_{in,1} + \Delta R_{in}}{R_{in,2} + \Delta R_{in}} \cdot \frac{R_{in,2} + (\Delta R_{Tj,u} + \Delta R_{Lj,u})/2}{R_{in,1} + (\Delta R_{Tj,u} + \Delta R_{Lj,u})/2} \quad (5)$$

The predicted incipient jet spacings, w_{jet}^* , of rings with increasing D_{in} based on $w_{jet}^*(\hat{D}_{in} = 200)$ agree well with those derived from the DEM simulations (see Fig. 11).

7. Discussion

In contrast with the quasi-static granular fingering which is dominated by the viscous forces [14–17], fast moving particle jetting is kinetically driven by the heterogeneous and erratic network of force chains which is intrinsically dictated by the particle packing. The present work reveals how the particle-scale heterogeneities of momentum brought in by the random network of force chains evolve into a consistent pattern containing the periodically spaced localized flows, namely the incipient jets. Theoretically predicting the pattern of incipient jets is much more challenging, involving characterizing the heterogeneities of the force networks which may change from packing to packing, and modeling the growth of and the interplay between neighboring localized flows. Some localized flows grow much faster than others. Meanwhile they interplay and compete with each other via the laterally deflected force chains across the width of the jamming front, leading to the shift, coalescence and annihilation of localized flows. The interplay among localized flows persists throughout the whole unjamming process until a well-defined pattern emerges.

Since the force structure and the unjamming dynamics of shock jammed particle layer determine the inception of the jetting pattern, among the most pertinent parameters are hardness of particles, coefficient of restitution (COR) and surface friction. Clark, et al. observed

Table 1

Correlation coefficients of $\Delta\hat{R}_{in}(\theta)$ of the internal perimeters of rings subjected to loads with different Δp_0 .

Δp_0	0.5	1.7	5	10
Δp_0				
0.5	1	0.3687	0.4380	0.3006
1.7	0.3687	1	0.4643	0.4953
5	0.4380	0.4643	1	0.5691
10	0.3006	0.4953	0.5691	1

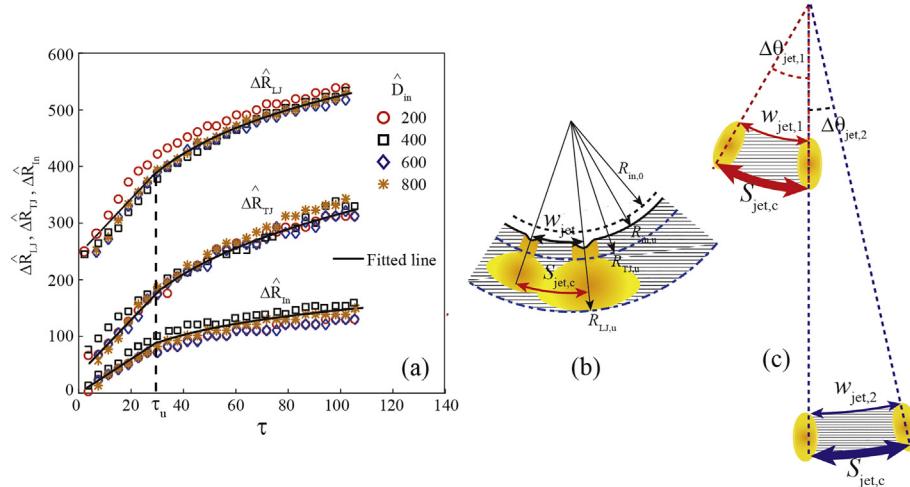


Fig. 12. (a) Trajectories of normalized displacements of the internal surfaces of rings, $\hat{\Delta R}_{in}$, the leading and trailing edges of the jamming fronts, $\hat{\Delta R}_{LJ}$ and $\hat{\Delta R}_{TJ}$, for rings with different D_{in} . (b) Illustration of the interplay between neighboring localized flows at the onset of unjamming. (c) Comparison of incipient jet spacing for rings with two different D_{in} .

that the force structure changes from the dense network to the sparse chains when particles become increasingly harder [24]. This finding suggests that the soft particles are inclined to move collectively, resembling the viscous fluid flows. By contrast, the discrete nature of particles is better manifested by the localized flows in hard particle systems. Our experiments do reveal a viscous stout finger-like jetting pattern in shocked flour rings as opposed to the radial crack-like jetting pattern in shocked sand rings [12]. COR and surface friction dictate the energy dissipation during the particle collision. Huang et al. found the profile of granular shock wave is affected by the COR and surface friction [20]. The scattering angle of the cone-shaped granular film formed by dense granular jets impacting a flat target is also found to depend on COR [21]. Therefore COR and surface friction may well affect the dynamics of unjamming process which involves the energy dissipation within the granular vortices. Recognizing the effects of these parameters on jetting pattern is of essence to modulate the emergent jetting pattern.

Although the particle jetting studied here is physically distinct from the multiple fractures of solid shells/rings subjected to the divergent impulsive loads [25], we can draw an analogue between the onset of unjamming in particles and the nucleation of defects in solids, as well as between the interplays among localized flows in particles and interactions among shear bands or micro-cracks in solids. For the former, the spatial and temporal statistics of the heterogeneities of momentum in shocked particles, analogous to the statistics of defects in solids, serves the starting point to predicting the jet pattern. Likewise the interplays between the localized flows stemming from the momentum heterogeneities can be modeled in light of the interaction between shear bands or micro cracks in solids. Opposed to the arrest of potential fractures in solids by the relaxation waves released by the neighboring fractures [25], the growth of minor localized flows is retarded by the “compaction waves” due to the collision of transverse flows. The propagating speed of the “compaction wave” is a function of a variety of factors, specifically the intensity of localized flows, packing fraction, material properties and loading strength. Quantitatively characterizing the statistics of the heterogeneities across the width of the jamming front and modeling the interplay between localized flows should be subjects of the following work.

8. Conclusion

DEM simulations of quasi-two-dimensional particle jetting, which are validated by the corresponding experimental results, reveal the physics governing the inception of jets. Without the presence of any

ab initio instabilities in the particle packing, the heterogeneous network of force chains, specifically the branched protruding force chain agglomerates across the width of the jamming front, instead introduce the momentum and packing heterogeneities which evolve into localized flows. These randomized and localized flows interact with each other via the vortex-like counter flows between them, leading to the shift, coalescence and annihilation of localized flows. As a result, a persisting pattern consisting of periodically spaced incipient jets emerges. The results presented in this paper contribute to fundamentally understand the physical principles behind particle jet formation in granular media and to improve and enable applications related to the explosive and shock induced jetting.

Acknowledgements

This work was supported by the National Natural Science Foundation of China (No. U1730111).

Appendix A. Formulation of the Hertz-Mindlin contact model

The Hertz-Mindlin contact model is a variant of the non-linear spring-dashpot contact model based on the Hertz-Mindlin contact theory. For two spherical particles in contact, i and j , the forces between them, F_c , consists of the normal and tangential components, namely F_n and F_t , which are composed of non-linear elastic and viscous damping elements as calculated by the equations as follows.

$$F_n = k_n \delta_n - \gamma_n \Delta V_n \quad (A.1)$$

$$F_t = \begin{cases} k_t \delta_t - \gamma_t \Delta V_t & \text{if } F_t < \mu_s F_n \\ \frac{\mu_s |k_n \delta_n| \delta_t}{|\delta_t|} & \end{cases} \quad (A.2)$$

The F_t becomes constant once the F_t calculated by the first expression of Eq. (A.2) is beyond the Coulomb friction limit governed by the product of the sliding friction coefficient μ_s and F_n . In Eqs. (A.1–A.2), δ_n is the overlap distance of particle i and j , $\delta_n = R_i + R_j - l_{ij}$, where R_i and R_j are the radii of the particles, i and j , respectively, l_{ij} is the distance between the centers of two particles. δ_t is the tangential displacement between two particles in contact for the contact duration. k_n and k_t are the stiffnesses for the normal and tangential contact, respectively. γ_n and γ_t are the viscoelastic damping constants for the normal and tangential contact, respectively. ΔV_n and ΔV_t are the normal and tangential components of the relative velocity of particles in contact, respectively.

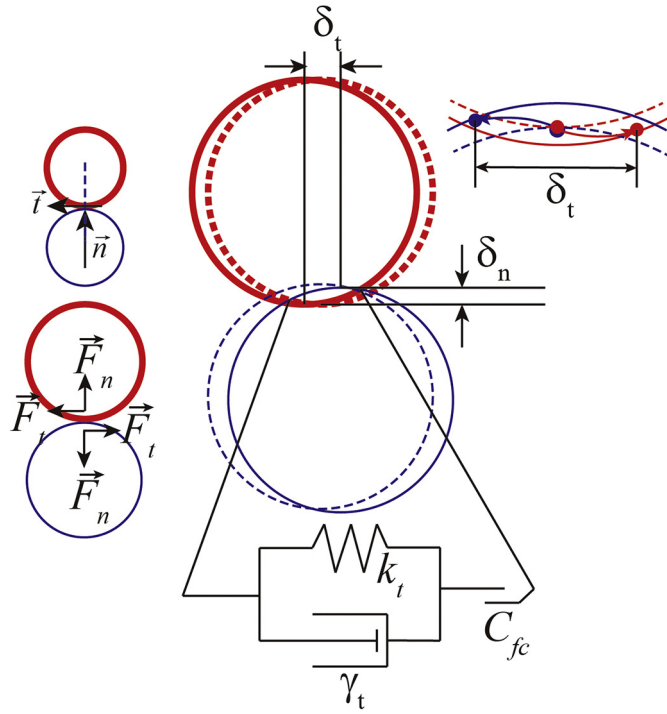


Fig. 13. Illustration of the δ_n , δ_t in the Hertz-Mindlin contact model. The insets show the directions of \vec{n} , \vec{t} , \vec{F}_n and \vec{F}_t .

Fig. 13 illustrates the δ_n , δ_t at one instant during the contact process of two spheres. Compared with the explicit definition of the δ_n , the derivation of the δ_t appears subtler. First we calculate the tangential component of the velocity of particle j relative to particle i at the contact point, $\Delta V_{t,C}$, by Eqs. (A.3) and (A.4).

$$\Delta V_{t,C} = \Delta \vec{V}_C \cdot \vec{t} \quad (\text{A.3})$$

$$\vec{t} = \frac{\Delta \vec{V}_C - (\Delta \vec{V}_C \cdot \vec{n}) \vec{n}}{|\Delta \vec{V}_C - (\Delta \vec{V}_C \cdot \vec{n}) \vec{n}|} \quad (\text{A.4})$$

where $\Delta \vec{V}_C$ is the velocity of particle j relative to particle i at the contact point, \vec{n} is the unit vector normal to the tangent plane of two particles through the contact point, \vec{t} is the unit vector align with the direction of $\Delta \vec{V}_{t,C}$. The δ_t is the integration of $\Delta V_{t,C}$ from the time when the two particles first came into contact, t_0 , to the current time, t (see Eq. (A.5)).

$$\delta_t = \int_{t=t_0}^{t=t} \Delta V_{t,C} dt \quad (\text{A.5})$$

The \vec{F}_n is the repulsive force perpendicular to the tangent plane at the contact point of two spheres. The \vec{F}_t is in the tangent plane and perpendicular to \vec{n} . **Fig. 13** also illustrates the directions of \vec{F}_n and \vec{F}_t . Note that the unit tangential direction, \vec{t} , may change during the contact as well as \vec{n} .

Table 2
Values of parameters used in the simulations.

Parameters	Values
Particle density, ρ_p	2700 kg/m ³
Wall density, ρ_w	7800 kg/m ³
Young's modulus of particles, Y_p	71.9 GPa
Young's modulus of walls, Y_w	200 GPa
Restitution Coefficient of particles, ε_p	0.7
Restitution Coefficient of walls, ε_w	0.9
Poisson ratio of particles, ν_p	0.3
Poisson ratio of walls, ν_w	0.27
Sliding friction coefficient of particles, μ_s	0.7
Sliding friction coefficient of walls, μ_w	0.3

The coefficients k_n , k_t , γ_n and γ_t are calculated using Eq. (A.6)

$$\left\{ \begin{array}{l} k_n = \frac{4}{3} Y_{ij}^* \sqrt{R_{ij}^* \delta_{nij}} \\ k_t = 8 G_{ij}^* \sqrt{R_{ij}^* \delta_{nij}} \\ \gamma_n = -2 \sqrt{\frac{5}{6}} \beta \sqrt{S_{ij,n} m_{ij}^*} \\ \gamma_t = -2 \sqrt{\frac{5}{6}} \beta \sqrt{S_{ij,t} m_{ij}^*} \end{array} \right. \quad (\text{A.6})$$

where Y_{ij}^* , R_{ij}^* , G_{ij}^* , β , $S_{ij,n}$, $S_{ij,t}$ and m_{ij}^* all are the function of the material's properties. The relations between these parameters and the material's properties are given by Eq. (A.7)

$$\left\{ \begin{array}{l} \frac{1}{Y_{ij}^*} = \frac{(1-\nu_i^2)}{Y_i} + \frac{(1-\nu_j^2)}{Y_j} \\ \frac{1}{G_{ij}^*} = \frac{2(2-\nu_i)(1+\nu_i)}{Y_i} + \frac{2(2-\nu_j)(1+\nu_j)}{Y_j} \\ S_{ij,n} = 2Y_{ij}^* \sqrt{R_{ij}^* \delta_{nij}} \\ S_{ij,t} = 2G_{ij}^* \sqrt{R_{ij}^* \delta_{nij}} \\ \beta = \frac{\ln \varepsilon}{\sqrt{\ln^2(\varepsilon) + \pi^2}} \end{array} \right. \quad (\text{A.7})$$

where Y is the Young's modulus, G is the shear modulus, ν is the Poisson ratio, ε is the coefficient of restitution. The effective R_{ij}^* and m_{ij}^* can be calculated from the radii and masses of the particles in contact:

$$\left\{ \begin{array}{l} \frac{1}{R_{ij}^*} = \frac{1}{R_i} + \frac{1}{R_j} \\ \frac{1}{m_{ij}^*} = \frac{1}{m_i} + \frac{1}{m_j} \end{array} \right. \quad (\text{A.8})$$

Table 2 lists the physical parameters adopted in the simulations

According to Ji and Shen [26], the time step should be less than 2% of the shortest binary contact time. Rayleigh and Hertz times, Δt_r and Δt_h , defined in Eq. (A.9) are taken as the estimates of the binary contact time.

$$\begin{aligned} \Delta t_r &= \pi R \sqrt{\frac{\rho}{G}} / (0.1631\nu + 0.8766) \\ \Delta t_h &= 2.87 \left(m^*{}^2 / R^* \cdot Y^*{}^2 \cdot V_{\max} \right)^{0.2} \end{aligned} \quad (\text{A.9})$$

In Eq. (A.9) V_{\max} is the maximum relative velocity of two particles in contact. Rayleigh time Δt_r is calculated for each particle in the simulation. Hertz time Δt_h is estimated by testing a collision of each particle with itself using V_{\max} as the assumed collision velocity. Throughout the simulations, the specified time step remains less than 1% of the minimum value of Δt_r and Δt_h .

We performed constant NVE integration based on velocity-Verlet integration scheme to update position, velocity, and angular velocity for finite-size spherical particles.

References

- [1] D.L. Frost, J. Loiseau, S. Goroshin, F. Zhang, A. Milne, A. Longbottom, Fracture of explosively compacted aluminum particles in a cylinder, *AIP Conf. Proc.* 1793 (1) (2017) 120019.
- [2] D.L. Frost, J. Loiseau, B.J. Marr, S. Goroshin, Particle segregation during explosive dispersal of binary particle mixtures, *AIP Conf. Proc.* 1793 (1) (2017) 120020.
- [3] K. Xue, F. Li, C. Bai, Explosively driven fragmentation of granular materials, *Eur. Phys. J. E* 36 (8) (2013) 1.
- [4] V. Rodriguez, R. Saurel, G. Jourdan, L. Houas, Solid-particle jet formation under shock-wave acceleration, *Phys. Rev. E* 88 (6) (2013), 063011.
- [5] L.F. David, G. Yann, P. Oren, G. Samuel, Z. Fan, Particle jet formation during explosive dispersal of solid particles, *Phys. Fluids* 24 (9) (2012), 091109.
- [6] A. Milne, C. Parrish, I. Worporland, Dynamic fragmentation of blast mitigants, *Shock Waves* 20 (1) (2010) 41.
- [7] A.M. Milne, E. Floyd, A.W. Longbottom, P. Taylor, Dynamic fragmentation of powders in spherical geometry, *Shock Waves* 24 (5) (2014) 501.
- [8] V. Rodriguez, R. Saurel, G. Jourdan, L. Houas, Impulsive dispersion of a granular layer by a weak blast wave, *Shock Waves* 27 (2) (2017) 187.
- [9] Z.-H. Shi, W.-F. Li, W.-W. Qian, H.-F. Liu, F.-C. Wang, Liquid-like granular film from granular jet impact, *Chem. Eng. Sci.* 162 (2017) 1.
- [10] R.C. Ripley, F. Zhang, Jetting instability mechanisms of particles from explosive dispersal, *J. Phys. Conf. Ser.* 500 (15) (2014), 152012.
- [11] K. Xue, Q. Yu, C. Bai, Dual fragmentation modes of the explosively dispersed granular materials, *Eur. Phys. J. E* 37 (2014) 88.
- [12] K. Xue, K. Du, X. Shi, Y. Gan, C. Bai, Dual hierarchical particle jetting of a particle ring undergoing radial explosion, *Soft Matt.* (2018), <https://doi.org/10.1039/c8sm00209f>.
- [13] K. Xue, L. Sun, C. Bai, Formation mechanism of shock-induced particle jetting, *Phys. Rev. E* 94 (2) (2016), 022903.
- [14] X. Cheng, L. Xu, A. Patterson, H.M. Jaeger, S.R. Nagel, Towards the zero-surface-tension limit in granular fingering instability, *Nat. Phys.* 4 (3) (2008) 234.
- [15] B. Sandnes, E.G. Flekkøy, H.A. Knudsen, K.J. Måløy, H. See, Patterns and flow in frictional fluid dynamics, *Nat. Commun.* 2 (2011) 288.
- [16] H. Huang, F. Zhang, P. Callahan, J. Ayoub, Granular fingering in fluid injection into dense granular media in a Hele-Shaw Cell, *Phys. Rev. Lett.* 108 (25) (2012), 258001.
- [17] C.W. MacMinn, E.R. Dufresne, J.S. Wettlaufer, Fluid-driven deformation of a soft granular material, *Phys. Rev. X* 5 (1) (2015) 011020.
- [18] P.A. Cundall, O.D.L. Strack, A discrete numerical model for granular assemblies, *Geotechnique* 29 (1979) 47.
- [19] H.P. Zhu, Z.Y. Zhou, R.Y. Yang, A.B. Yu, Discrete particle simulation of particulate systems: theoretical developments, *Chem. Eng. Sci.* 62 (13) (2007) 3378.
- [20] Y.J. Huang, P. Jalali, T. Hyppanen, Numerical simulation of the formation of granular shock wave over cylindrical obstacle, *Part. Part. Sys. Charact.* 29 (2012) 128.
- [21] Y.J. Huang, C.K. Chan, P. Zamankhan, Granular jet impingement on a fixed target, *Phys. Rev. E* 82 (3) (2010), 031307.
- [22] W. Zhong, A. Yu, X. Liu, Z. Tong, H. Zhang, DEM/CFD-DEM modelling of non-spherical particulate systems: theoretical developments and applications, *Powder Technol.* 302 (Supplement C) (2016) 108.
- [23] S.R. Waitukaitis, L.K. Roth, V. Vitelli, H.M. Jaeger, Dynamic jamming fronts, *Europhys. Lett.* 102 (4) (2013), 44001.
- [24] A.H. Clark, A.J. Petersen, L. Kondic, R.P. Behringer, Nonlinear force propagation during granular impact, *Phys. Rev. Lett.* 114 (14) (2015), 144502.
- [25] D.E. Grady, *Dynamical Fragmentation of Solids*, Springer, Berlin Heidelberg, 2009.
- [26] S. Ji, H.H. Shen, Effect of contact force models on granular flow dynamics, *J. Eng. Mech.* 132 (2006) 1252–1259.